Growth, spectroscopy and laser operation of monoclinic Nd:$CsGd(MoO_4)_2$ crystal with a layered structure

Pavel Loiko[a], Anatoly Pavlyuk[b], Sami Slimi[c,d], Rosa Maria Solé[c], Ezzedine Ben Salem[d], Elena Dunina[e], Alexey Kornienko[e], Patrice Camy[a], Uwe Griebner[f], Valentin Petrov[f], Francesc Díaz[c], Magdalena Aguiló[c], and Xavier Mateos[c,*]

[a]*Centre de Recherche sur les Ions, les Matériaux et la Photonique (CIMAP), UMR 6252 CEA-CNRS-ENSICAEN, Université de Caen Normandie, 6 Boulevard du Maréchal Juin, 14050 Caen Cedex 4, France*
[b]*A. V. Nikolaev Institute of Inorganic Chemistry, Siberian Branch of Russian Academy of Sciences, 3 Lavrentyev Ave., Novosibirsk 630090, Russia*
[c]*Física i Cristal·lografia de Materials i Nanomaterials (FiCMA-FiCNA)-EMaS, Dept. Química Física i Inòrganica, Universitat Rovira i Virgili (URV), Campus Sescelades, E-43007 Tarragona, Spain*
[d]*I.P.E.I. of Monastir, Unit of Materials and Organic Synthesis Monastir 5019, UR17ES31, Tunisia*
[e]*Vitebsk State Technological University, 72 Moskovskaya Ave., 210035 Vitebsk, Belarus*
[f]*Max Born Institute for Nonlinear Optics and Short Pulse Spectroscopy, Max-Born-Str. 2a, D-12489 Berlin, Germany*

**Corresponding author, e-mail: xavier.mateos@urv.cat*

Abstract. We report on the growth, structure, polarized spectroscopy and first laser operation of a double molybdate compound featuring a layered structure – the monoclinic Nd:$CsGd(MoO_4)_2$. Single-crystals of 3 at.% Nd:$CsGd(MoO_4)_2$ are grown from the flux using cesium trimolybdate ($Cs_2Mo_3O_{10}$) as a solvent. They crystallize in the monoclinic system (sp. gr. $P2/c$) with lattice constants a = 9.5239(4) Å, b = 5.0752(5) Å, c = 8.0580(7) Å and β = 91.157(9)°. Nd:$CsGd(MoO_4)_2$ exhibits a perfect cleavage along the (100) plane. Polarized absorption and luminescence spectra of the Nd^{3+} dopant ion are measured. The maximum stimulated-emission cross-section is 29.0×10^{-20} cm^2 at 1065.9 nm for light polarization $\boldsymbol{E} \parallel \boldsymbol{b}$. The luminescence lifetime is 145 μs. The transition probabilities are determined using the modified Judd-Ofelt theory yielding the intensity parameters Ω_2 = 26.736, Ω_4 = 12.736 and Ω_6 = 17.771 [10^{-20} cm^2] and α = 0.122 [10^{-4} cm]. Continuous-wave laser operation is achieved in cleaved single-crystal plates of Nd:$CsGd(MoO_4)_2$ yielding a maximum output power of 0.54 W at 1066 nm with a laser threshold of 70 mW, a slope efficiency η of 60.4% and a linearly polarized laser output ($\boldsymbol{E} \parallel \boldsymbol{b}$).

Keywords: double molybdate crystals, layered structure, neodymium ions, spectroscopy, laser operation.

1. Introduction

The crystal family of alkali (M^+) rare earth (M^{3+}) double tungstates / molybdates with a general chemical formula of $M^+M^{3+}(XO_4)_2$ (where X = W or Mo, respectively) [1], is known to be very suitable for doping with active rare-earth ions (RE^{3+}) for laser applications [2]. These crystals offer a broad variety of structural types (including disordered materials) [3] and they possess several important advantages. First, they have a substitutional rare-earth site (M^{3+}) facilitating their doping by the laser-active RE^{3+} ions in high concentrations [4]. Second, they typically provide strong anisotropy of the spectroscopic properties for polarized light [5,6]. Third, relatively large M^{3+} - M^{3+} interatomic distances reduce the energy migration between the active RE^{3+} ions and impurity centers leading to weak concentration quenching (moreover, non-radiative relaxations in these crystals can be weak) [7]. Finally, the considered materials are Raman-active [8].

A prominent example is the class of the monoclinic potassium rare-earth double tungstates, $KRE(WO_4)_2$ (RE = Gd, Y or Lu) [2]. These crystals were extensively studied for doping with RE^{3+} ions such as Nd^{3+} [9], Yb^{3+} [10], Tm^{3+} [11] or Ho^{3+} [12] giving rise to efficient laser emissions in the near-infrared (1–2 μm). In particular, Nd:$KGd(WO_4)_2$ is a very suitable medium for compact low-threshold and efficient lasers at 1067 and 1351 nm (the $^4I_{9/2} \rightarrow {}^4I_{11/2}$ and $^4I_{13/2}$ transitions of Nd^{3+}) [13-15]. Self-Raman conversion of the latter transition leads to eye-safe emission while the frequency-doubling paved the way towards yellow lasers [16-18]. Note that Gd^{3+} has been selected as a host-forming cation for Nd^{3+} doping because of the closeness of their ionic radii and, thus, better crystal quality and higher available doping levels. The drawback of Nd:$KGd(WO_4)_2$ is the strongly anisotropic thermal lensing which is negative for the conventional crystal cut (along the growth direction) [15].

Among the alkali rare-earth double tungstate / molybdate crystals, cesium (Cs) based compounds have been rarely studied [19,20]. It is known that such crystals possess “loose” structures giving rise to such features as strong acousto-optic coupling [21], high magnetic anisotropy [22] or mica-like natural cleavage [20] which are of interest for multiple applications. For example, crystals with a layered structure offer strong anisotropy of the spectroscopic properties and easy mechanical cleavage being promising for thin-film and microchip lasers [23,24]. The class of the cesium rare-earth double molybdates, $CsRE(MoO_4)_2$ is such an example [1]. These compounds crystallize in the monoclinic system (for RE = Ce – Lu, sp. gr. *P*2/*c*) [19]. As for Nd^{3+} doping, the most attractive representative is $CsGd(MoO_4)_2$.

So far, only few studies were dedicated to $CsGd(MoO_4)_2$ type crystals. Klevtsova *et al.* briefly described the crystalline structure of the stoichiometric $CsPr(MoO_4)_2$ crystal which is a representative of the structural type for RE = Ce – Lu [25]. Ivannikova *et al.* reported on the growth of undoped $CsGd(MoO_4)_2$ crystals by the Kyropoulos and Czochralski (Cz) methods and discussed the possible solvents to be used [21]. The various structural types of $CsR(MoO_4)_2$ (R = La – Lu, In, Sc, Fe, Cr, Al) crystals were summarized by Klevtsov *et al.* [1]. Pavlyuk *et al.* reported on laser emission from a stoichiometric $CsNd(MoO_4)_2$ crystal under pulsed pumping by a Ruby laser [26]. Only the wavelength of the stimulated emission (1065.8 nm) and the laser threshold (49 mJ) under ns pulse excitation were provided. The

crystalline structure of this material leading to a weak concentration quenching, allowed for laser emission with such high Nd^{3+} content (100 at.%). Note that in these early studies, the structural type of $CsPr(MoO_4)_2$ was assigned as orthorhombic.

In recent years, the interest in $CsGd(MoO_4)_2$ crystals has increased. Zhao *et al.* reported on the growth and polarized optical spectroscopy of Yb^{3+}-doped $CsGd(MoO_4)_2$ [20]. The authors also predicted the suitability of $CsGd(MoO_4)_2$ crystals for microchip lasers based on mechanically cleaved crystalline plates; however, no laser operation was achieved. The magnetic properties of bulk $CsGd(MoO_4)_2$ crystals were studied for application in single ion magnets [22,27]. The heat capacity and thermal conductivity of bulk $CsGd(MoO_4)_2$ were measured at cryogenic temperatures [28,29]. $CsGd(MoO_4)_2$ nanopowders doped with Dy^{3+} [30], Eu^{3+} [19] and Er^{3+}/Ho^{3+} [31] ions were also studied recently for applications as phosphors in light emitting diodes (LEDs).

In the present work, we report on the growth, structure refinement, polarized optical spectroscopy and continuous-wave laser operation of Nd^{3+}-doped monoclinic cesium gadolinium double molybdate crystal with layered structure - $Nd:CsGd(MoO_4)_2$.

2. Crystal growth

$CsGd(MoO_4)_2$ melts incongruently at 1308 K. Although it does not exhibit polymorphism, it decomposes at high temperatures according to the equation: $2CsGd(MoO_4)_2 \rightarrow Gd_2MoO_6$ (s) + $Cs_2Mo_3O_{10}$ (l) where (s) and (l) stand for solid and liquid phase, respectively. Consequently, in the present work, bulk $Nd:CsGd(MoO_4)_2$ crystals were grown from the flux under low thermal gradients (LTG). This method is referred to as modified Czochralski LTG method in the Russian literature. Cesium trimolybdate ($Cs_2Mo_3O_{10}$) was selected as a solvent. $CsGd(MoO_4)_2$ can be grown using several solvents, i.e., Cs_2MoO_4, $Cs_2Mo_2O_7$ and $Cs_2Mo_3O_{10}$. It has good solubility in all of them. However, according to the phase diagram of the $2CsGd(MoO_4)_2 – Cs_2MoO_4$ system [21], the crystallization area of cesium gadolinium molybdate is limited by the eutectic with only 30 mol% $CsGd(MoO_4)_2$ melting at 1023 K. Among $Cs_2Mo_2O_7$ and $Cs_2Mo_3O_{10}$, the latter is more favorable for the single-crystal growth. Both solvents show a similar range of crystallization of $CsGd(MoO_4)_2$, but the latter is less volatile and provides better crystal quality with less impurities.

The molar ratio of the solute / solvent $Nd:CsGd(MoO_4)_2 – Cs_2Mo_3O_{10}$ was selected to be 85 – 15 mol%. The raw materials were Cs_2CO_3 (purity: 99.995%), Gd_2O_3, Nd_2O_3 (both 99.999%) and MoO_3 (99.9992%). The concentration of Nd^{3+} in the solute material was set to 5 at.% (the Nd^{3+} ions replace the Gd^{3+} ones). To ensure the molar ratio, Cs_2CO_3 and MoO_3 were added in excess to the stoichiometry in such a way that the starting concentration of cesium trimolybdate in the solution ($Cs_2Mo_3O_{10} = Cs_2CO_3 + 3Mo_3$) did not exceed 20 mol%. The raw materials were weighed, mixed and placed in a Pt crucible (diameter: 70 mm, height: 120 mm). The growth was performed in air. First, the crucible was slowly heated up to 1298 K at a rate of 200 K/h and kept at this temperature for 20–25 h under constant stirring to homogenize the solution. As the used cesium compounds are volatile, higher temperatures are undesirable. Then, the temperature was reduced down to the saturation temperature of the solution (1288 K, see Fig. 1). A seed fixed to a Pt holder was lowered towards the surface of

the solution. The rotation speed was 30 rev / min, the pulling rate was 0.5–3 mm/day and the cooling rate was 1–2 K / day. This led to a growth rate of 1–3 g/day. The temperature gradients in the solution were as following: <1 K/cm in the radial direction and <5-10 K/cm in the axial one. After 5–10 days of growth, the crystal was removed from the solution and slowly cooled down to room-temperature at a rate of 15 K / hour. No post-growth annealing was applied.

To fabricate the seeds, undoped crystal blocks were grown using a Pt wire. From these samples, we obtained single-crystalline pieces by mechanical cleavage. They were further oriented using single-crystal X-ray diffraction along the [100], [010] or [001] axes.

As an example, a Nd:$CsGd(MoO_4)_2$ crystal (further abbreviated as Nd:CsGdMo) grown using a [001]-oriented seed is shown in Fig. 2(a). It is clear, transparent and free of cracks. The crystal boule has a cylindrical shape and a slight violet coloration due to the Nd^{3+} doping (undoped CsGdMo crystals grown by the same method are colorless). The crystals exhibit a perfect natural mica-like cleavage along the (100) plane. The crystals were optically homogeneous, as revealed by their illumination by a He-Ne laser showing no scattering centers.

The segregation coefficient for Nd^{3+} ions, $K_{Nd} = C_{crystal}/C_0$, where $C_{crystal}$ and C_0 are the doping levels in the crystal / raw materials, respectively, was estimated using an Electron Probe Micro-Analyzer (EPMA, JEOL, model JXA-3) and was in the range of 0.6-0.7±0.1, depending on the growth rate. For the Nd:CsGdMo crystal used for the spectroscopic and laser studies, the actual doping level was 3.0±0.3 at.% ($CdGd_{0.97}Nd_{0.03}(MoO_4)_2$), or, equivalently, the ion concentration N_{Nd} was $1.51\pm0.15\times10^{20}$ cm^{-3}. The determined segregation coefficient for Nd^{3+} ions is lower than that for Yb^{3+} ions in the same host material, $K_{Yb} = 0.88$ [20], which is probably due to the different growth conditions.

Due to the layered crystal structure, the thermal conductivity of CsGdMo is anisotropic. Because of this, the morphological stability of growth along the [010] or [001] directions is high. If grown along the [100] axis, the crystals exhibit a varying cross-sectional shape, Fig. 2(b).

For crystals grown along the [010] and [001] directions, the face oriented towards the flux surface is smooth (circular) indicating a normal growth mechanism. For crystals grown along the [100] direction, this face is determined by the (100) plane (a mixed growth mechanism). We believe that the latter is the main reason for mechanical stresses and defects during the growth of doped crystals.

3. Experimental

Structural characterization of Nd:$CsGd(MoO_4)_2$ was carried out by the X-ray powder diffraction (XRD) technique. The measurements were performed in a θ - θ Brag Brentano configuration using a Siemens D-5000 powder X-ray diffractometer with Cu Kα (1.5406 Å) radiation. For structure refinements, the XRD pattern was recorded in a 2θ range from 10º to 70º, a step time of 16 s and a step size of 0.02º. The same XRD equipment with a temperature chamber (HTK10) was used to collect X-ray powder diffraction data at different temperatures from 303 K to 823 K in the same 2θ range as mentioned above, but with a step time of 5 s, a

step size of 0.03º and a delay of 300 s before each measurement. The heating rate from one measurement temperature to the next one was 0.17 K/s.

All spectroscopic studies were performed at room temperature (RT, 293 K). The absorption spectra were measured using a spectrophotometer (Lambda 1050, Perkin Elmer) and a Glan-Taylor polarizer. The spectral resolution was 0.5 nm. The luminescence spectra were measured using an optical spectrum analyzer (OSA, Ando AQ6315-E) and a Glan-Taylor polarizer. As an excitation source, we used a CW Ti:Sapphire laser tuned to ~0.81 μm. The OSA was calibrated using a 20 W quartz iodine lamp.

The luminescence decay was studied using a 1/4 m monochromator (Oriel 77200) and an InGaAs detector. The Nd^{3+} luminescence was excited by the output of a nanosecond optical parametric oscillator (OPO, Horizon, Continuum) tuned to ~0.81 μm. The luminescence decay curve was fitted with a single-exponential law, $I_{lum}(t) = I_0\exp(-t/\tau_{lum})$.

4. Results and discussion

4.1. Crystal structure

The measured XRD pattern of 3 at.% Nd:CsGdMo obtained for the structure refinement is shown in Fig. 3. First, we tried to perform the Rietveld refinement of the structure with the TOPAS software considering the preferential orientation of (100). We observed that the width of the diffraction peaks of different families of planes (namely, the (h 0 0), (h 0 h) and (2h 0 h) ones) was different. As the CsGdMo crystals are soft (Mohs hardness: <2), this can be in part explained by their deformation during the growth. Thus, it was not possible to obtain a good Rietveld refinement, even by separate fitting of the different families of peaks that have different widths.

We could only obtain the unit cell parameters using the Le Bail method [32]. The initial unit cell parameters for the Le Bail refinement were taken from [19]. Nd:CsGdMo is monoclinic (sp. gr. $P2/c$ – C^4_{2h}, No. 13, point group $2/m$). The lattice constants are a = 9.5239(4) Å, b = 5.0752(5) Å, c = 8.0580(7) Å and the monoclinic angle $\beta = \boldsymbol{a}\hat{}\boldsymbol{c}$ = 91.157(9)° (the number of the structural units Z = 2). The theoretical crystal density ρ_{calc} = 5.198 g/cm^3. The R-factors were R_{exp} = 6.54 and R_{wp} = 8.52 (the reduced chi-squared value $\chi^2 = (R_{wp}/R_{exp})^2$ = 1.70). No other phases apart from the monoclinic one were found. The XRD pattern is in good agreement with the ICSD PDF card #01-083-5116 for undoped CsGdMo with monoclinic structure (a = 9.5289 Å, b = 5.0823 Å, c = 8.0563 Å and β = 91.246°) [19]. Note that in the early papers, the structure of CsGdMo was assigned to the orthorhombic system (sp. gr. $Pbmb$ = D^3_{2h}) probably because of the closeness of β to the right angle. Indeed, Klevtsova *et al.* reported the following lattice constants for an isostructural CsPrMo crystal: a = 9.56 Å, b = 5.14 Å, c = 8.26 Å and β = 90° [25], with the same assignment of crystallographic axes as obtained in the present work. Figure 3 shows the observed, calculated (Le Bail method) and residual powder XRD patterns. The peaks were indexed according to the ICSD PDF card number 01-083-5116.

The structure of Nd:CsGdMo is shown in Fig. 4 (for the atomic coordinates from [19]). CsGdMo is an ordered crystal. The Cs^+ and $Gd^{3+}|Nd^{3+}$ cations are located in different sites (Wyckoff symbols: 2*f* and 2*e*, respectively) with VIII-fold oxygen coordination. The Gd|Nd–

O interatomic distances for the [Gd|NdO_8] square antiprisms are in the range of 2.27–2.70 Å. The Mo^{6+} cations are located in distorted [MoO_4] tetrahedra (the Mo–O interatomic distances: 1.53–2.07 Å). The edge-sharing [Gd|NdO_8] square antiprisms form layers in the ***b*-*c*** plane which are connected to the [MoO_4] tetrahedra through the oxygen atoms. In the direction orthogonal to the layer plane (along the ***a***-axis), the layers are isolated (separated by the distance *a*) and they are connected only by the [CsO_8] polyhedra (Cs–O interatomic distances: 2.80–3.39 Å). Thus, the stacking of alternating layers – [Gd|NdO_8] - [MoO_4] – Cs – [MoO_4] - [Gd|NdO_8] – occurs along the crystallographic ***a***-axis. Each layer is parallel to the (100) plane which explains the cleavage feature. The Nd^{3+} ions substitute for the Gd^{3+} ones in 2*e* sites (local site symmetry: C_2). This process is favored by the closeness of their ionic radii, R_{Nd} = 1.109 Å and R_{Gd} = 1.053 Å (for VIII-fold coordination). The shortest Gd|Nd – Gd|Nd interatomic separations are observed in the layer plane: 4.05 Å and 5.08 Å along the ***c***- and ***b***-axes, respectively. In the orthogonal direction, the shortest separation is 9.52 Å. Such long interatomic separations (although not record high for stoichiometric Nd^{3+}-doped crystals) greatly suppress the cross-talk between Nd^{3+} ions leading to weak luminescence quenching.

The XRD patterns of Nd:CsGdMo recorded at temperatures from 303 K to 823 K were used to determine the linear thermal expansion tensor. This study is of great interest to predict the thermal behavior of this material in laser experiments. The unit cell parameters of Nd:CsGdMo at different temperatures were refined using the TOPAS software and the Le Bail method. Figure 5 shows the evolution of the relative elongations $\Delta L/L_0$ (where $L = a$, b, c and $c^* = c\times\cos(\beta - 90^\circ)$) of Nd:CsGdMo, as a function of temperature, taking as reference the unit cell parameters at 303 K (L_0). All the unit cell parameters increase linearly with temperature. The monoclinic angle β first slowly decreases in the temperature range of 303 – 773 K and then stabilizes around 90.30° for the high temperatures of 823 – 923 K. Thus, even at high temperatures, the Nd:CsGdMo crystal preserves its monoclinic structure with the β angle clearly above 90°. The linear thermal expansion coefficients are calculated in the given crystallographic direction $\alpha = (\Delta L/L_0)/\Delta T$ [33].

The linear thermal expansion tensor of this material in the crystallo-physical system (X_1 || ***a***, X_2 || ***b*** and X_3 || ***c****) is then obtained:

$$\alpha_{ij} = \begin{pmatrix} 31.80 & 0 & 0.05 \\ 0 & 9.98 & 0 \\ 0.05 & 0 & 26.70 \end{pmatrix} \times 10^{-6} \mathrm{K}^{-1}.$$

To obtain the linear thermal expansion tensor in the eigen frame (axes X'_1, X'_2 and X'_3), the previous tensor was diagonalized [34], yielding the following values:

$$\alpha_{ij} = \begin{pmatrix} 31.8 & 0 & 0 \\ 0 & 10.0 & 0 \\ 0 & 0 & 26.7 \end{pmatrix} \times 10^{-6} \mathrm{K}^{-1}.$$

The orientation of the thermal expansion tensor frame is as follows: X'_2 parallel to the ***b***-axis and the other two axes (X'_1 and X'_3) located in the orthogonal plane (the ***a*-*c*** plane). X'_1 is located at 0.54º from the ***a***-axis (clockwise) and X'_3 is located at 0.54º from the ***c****-axis (anticlockwise), with the ***b***-axis pointing towards the observer.

Note that the diagonal values in the two frames are almost equal, because β in the crystal structure is close to the right angle (90º) and the non-diagonal element α_{13} of the tensor in the crystallo-physical system is very small. During the diagonalization, the changes of the diagonal elements were within the error margin of the same values.

4.2. Judd-Ofelt analysis

The monoclinic Nd:CsGdMo crystal is optically biaxial. However, the assignment of its optical indicatrix axes is unknown, only a mean refractive index $\langle n \rangle \approx 1.95$ at the wavelength of 632 nm is known [26]. Thus, in the present work, we will refer to the principal light polarizations $\boldsymbol{E} \parallel \boldsymbol{a}, \boldsymbol{b}, \boldsymbol{c}$.

The polarized absorption spectra of Nd^{3+} ions in CsGdMo are shown in Fig. 6. The absorption bands assigned to transitions from the ground-state ($^4I_{9/2}$) to the excited-states from $^4F_{3/2}$ to $^2I_{11/2}$ are observed in the spectra. The UV absorption edge is at 328–343 nm, depending on the polarization (the bandgap E_g = 3.6–3.8 eV). It was determined from the so-called Tauc plot, i.e., by plotting $(\alpha_{abs} \times h\nu_{ph})^2$ versus the photon energy $h\nu_{ph}$ and extrapolating the linear part of the graph to the horizontal axis. This value is slightly smaller than determined previously for CsGdMo nanopowders (E_g = 4.13 eV) [30].

The transition probabilities of Nd^{3+} ions in the CsGdMo crystal were analyzed using the Judd-Ofelt (J-O) theory [36,37]. The calculations were performed using the standard J-O theory and its modifications accounting for configuration interaction: the modified Judd-Ofelt theory (mJ-O) [37] and the approximation of an intermediate configuration interaction (ICI) [38,39]. The reduced squared matrix elements $U^{(k)}$, k = 2, 4, 6 for transitions in absorption and emission were calculated using the free-ion parameters from [40]. The J-O formalism was applied to electric-dipole (ED) contributions to the intensities of the 4f-4f Nd^{3+} transitions. The contribution of magnetic-dipole (MD) transitions with $\Delta J = J - J' = 0, \pm 1$ was calculated separately within the Russell–Saunders approximation on wave functions of Nd^{3+} under the assumption of a free-ion.

For the standard J-O theory, the ED line strengths of the J → J' transitions $S^{ED}(JJ')$ are [35,36]:

$$S_{calc}^{ED}(JJ') = \sum_{k=2,4,6} U^{(k)} \Omega_k, \tag{1a}$$

$$U^{(k)} = \langle (4f^n) SLJ \| U^k \| (4f^n) S'L'J' \rangle^2. \tag{1b}$$

Here, $U^{(k)}$ are the reduced squared matrix elements and Ω_k are the intensity (J–O) parameters (for both, k = 2, 4, 6).

For the ICI approximation, the ED line strengths are given by [38]:

$$S_{calc}^{ED}(JJ') = \sum_{k=2,4,6} U^{(k)} \tilde{\Omega}_k, \tag{2a}$$

$$\tilde{\Omega}_k = \Omega_k [1 + 2R_k (E_J + E_{J'} - 2E_f^0)]. \tag{2b}$$

The J-O (intensity) parameters $\tilde{\Omega}_k$ are the linear functions of energies of the two multiplets (E_J and $E_{J'}$) involved in the transition, where E_f^0 is the mean energy of the $4f^n$ configuration

and R_k (k = 2, 4, 6) are the parameters representing the configuration interaction. There exist six free parameters, namely Ω_k and R_k (k = 2, 4, 6).

If only the excited configuration with opposite parity $4f^{n-1}5d^1$ contributes to the configuration interaction, $R_2 = R_4 = R_6$ are constant, defined as $\alpha \approx 1/(2\Delta)$, and a simpler expression for the J-O parameters is obtained:

$$S^{ED}_{calc}(JJ') = \sum_{k=2,4,6} U^{(k)} \tilde{\Omega}_k , \quad (3a)$$

$$\tilde{\Omega}_k = \Omega_k [1 + 2\alpha(E_J + E_{J'} - 2E^0_f)]. \quad (3b)$$

These equations are referred to as the mJ-O theory [37,38]. There exist four free parameters, namely Ω_2, Ω_4, Ω_6 and α. Δ means the energy of the excited configuration $4f^{n-1}5d^1$. Equation (3) is transformed into Eq. (1) assuming that the excited configuration of opposite parity has high energy ($\Delta \rightarrow \infty$, $\alpha \rightarrow 0$).

For the optically biaxial Nd:CsGdMo crystal, all the calculations were performed by averaging the polarizations, $<X> = (1/3)(X_a + X_b + X_c)$ where X is the parameter and a, b, c mark the polarization state. The measured and calculated absorption oscillator strengths ($<f^{\Sigma}_{exp}>$ and $<f^{\Sigma}_{calc}>$, respectively) are shown in Table 1. Here, the superscript "Σ" stands for the total (ED + MD) value. The root-mean-square (rms) deviation between these values is minimized when using the mJ-O theory (1.577) as compared to the standard J-O theory (1.654) and the ICI approximation (1.792). Moreover, the standard J-O theory provides a notably underestimated radiative lifetime of the $^4F_{3/2}$ state. Thus, we used the mJ-O model for further calculations. The determined intensity parameters ({Ω_k} for the J-O model, {Ω_k and α} for the mJ-O one and {Ω_k and R_k} for the ICI approximation) are listed in Table 2. For the mJ-O theory, Ω_2 = 26.74, Ω_4 = 12.74 and Ω_6 = 17.77 [10^{-20} cm^2] and α = 0.122 [10^{-4} cm]. Thus, Δ = 40980 cm^{-1}.

In Table 3, we compare the J-O parameters reported for Nd^{3+}-doped complex tungstate and molybdate crystals [5,41-46]. Kaminski has shown that the luminescence branching ratios for the $^4F_{3/2} \rightarrow {}^4I_{J'}$ transitions of Nd^{3+} ions depend mostly on the Ω_4 and Ω_6 parameters, which is expressed by the spectroscopic quality factor $X = \Omega_4/\Omega_6$ [47]. Lower X is favorable for the main transition of interest, $^4F_{3/2} \rightarrow {}^4I_{11/2}$. In our case, X = 0.72 (for the mJ-O theory). Previously, for complex tungstate and molybdate crystals, X values were determined in the 0.74-1.42 range.

Using the intensity parameters for the mJ-O theory, we analyzed the transition of interest for Nd^{3+} ions originating from the $^4F_{3/2}$ state and terminating at the lower-lying $^4I_{J'}$ (J' = 9/2 – 15/2) multiplets. The probabilities of spontaneous radiative transitions A(JJ'), the luminescence branching ratios B(JJ') and the radiative lifetime of the emitting state τ_{rad} are listed in Table 4. The τ_{rad} value is 136.86 ms. For the $^4F_{3/2} \rightarrow {}^4I_{11/2}$ transition giving rise to emission at ~1 μm, the luminescence branching ratio is 52.7%.

4.3. Transition cross-sections and emission lifetime

The absorption cross-sections were calculated from the measured absorption spectra, $\sigma_{abs} = \alpha_{abs}/N_{Nd}$. For Nd^{3+} ions, the transitions attractive for pumping are the $^4I_{9/2} \rightarrow {}^4F_{5/2}$ +

$^2H_{9/2}$ (at ~0.81 μm) and $^4F_{3/2}$ (at ~0.87 μm) ones. The corresponding σ_{abs} spectra are shown in Fig. 7.

The $^4I_{9/2} \rightarrow {}^4F_{5/2} + {}^2H_{9/2}$ absorption band is spectrally matching the emission of commercial AlGaAs laser diodes and is commonly used for pumping of Nd lasers (the so-called conventional pumping scheme). The maximum $\sigma_{abs} = 18.8\times10^{-20}$ cm^2 at 808.8 nm is for light polarization $\boldsymbol{E} \parallel \boldsymbol{b}$. The corresponding full width at half maximum (FWHM) of the absorption peak is 2.9 nm. A strong anisotropy of the absorption cross-sections is observed, i.e., $\sigma_{abs}(\boldsymbol{b}) : \sigma_{abs}(\boldsymbol{a}) = 4.4$ and $\sigma_{abs}(\boldsymbol{b}) : \sigma_{abs}(\boldsymbol{c}) = 22$ at this wavelength.

The $^4I_{9/2} \rightarrow {}^4F_{3/2}$ absorption band is nowadays attracting attention for the so-called in-band pumping directly to the upper laser level thus reducing the heat loading. The maximum $\sigma_{abs} = 8.2\times10^{-20}$ cm^2 occurs at 874.3 nm for light polarization $\boldsymbol{E} \parallel \boldsymbol{b}$ (FWHM = 3.2 nm).

The stimulated-emission (SE) cross-sections, σ_{SE}, for the $^4F_{3/2} \rightarrow {}^4I_{J'}$ ($J' = 9/2 – 13/2$) transition of Nd^{3+} ions were calculated using the Füchtbauer–Ladenburg (F-L) equation [48]:

$$\sigma_{SE}^{i}(\lambda)=\frac{\lambda^5}{8\pi<n>^2\tau_{rad}c\,(1/3)\sum\limits_{i=a,b,c}\int\lambda W_i(\lambda)\mathrm{d}\lambda}\frac{W_i(\lambda)B(JJ')}{}, \qquad (4)$$

where, λ is the light wavelength, $<n>$ is the mean refractive index, c is the speed of light, τ_{rad} is the radiative lifetime of the emitting state ($^4F_{3/2}$), $W_i(\lambda)$ is the luminescence spectrum for i-th polarization (i = a, b, c), and B(JJ') is the luminescence branching ratio of the transition. The results are shown in Fig. 8.

For the $^4F_{3/2} \rightarrow {}^4I_{11/2}$ transition, which is the most commonly used one for laser operation with Nd^{3+} doping, the maximum SE cross-section σ_{SE} is 29.0×10^{-20} cm^2 at 1065.9 nm for light polarization $\boldsymbol{E} \parallel \boldsymbol{b}$. The corresponding emission bandwidth (at FWHM) is 3.4 nm. The Nd:CsGdMo crystal shows a strong anisotropy of the SE cross-sections with polarized light determined by its layered structure. Indeed, $\sigma_{SE}(\boldsymbol{b}) : \sigma_{SE}(\boldsymbol{a}) = 2.5$ and $\sigma_{SE}(\boldsymbol{b}) : \sigma_{SE}(\boldsymbol{c}) = 2.1$ at the above wavelength. Such an anisotropy will determine a linearly polarized laser output. Other emission peaks are observed at 1056.9, 1074.8, 1083.3 and 1093.1 nm.

For the $^4F_{3/2} \rightarrow {}^4I_{13/2}$ and $^4I_{9/2}$ transitions, σ_{SE} reaches 4.82×10^{-20} cm^2 at 1347.3 nm (FWHM = 23.2 nm) and 3.50×10^{-20} cm^2 at 898.4 nm (FWHM = 13.2 nm), respectively.

The luminescence decay curve for the 3 at.% Nd:CsGdMo crystal is shown in Fig. 9. The luminescence decay is clearly single-exponential in agreement with a single type of sites for Nd^{3+} ions. The luminescence decay time τ_{lum} is 145±5 μs, in agreement with the calculated τ_{rad} value.

A comparison of the spectroscopic properties of Nd^{3+} ions in several known double tungstate (DT) and double molybdate (DMo) laser host crystals, namely $CsGd(MoO_4)_2$, $KY(MoO_4)_2$ [49] and $KGd(WO_4)_2$ [9], is given in Table 5. Among the crystal family of DTs / DMos, the Nd:CsGdMo crystal features the highest SE cross-section for the $^4F_{3/2} \rightarrow {}^4I_{11/2}$ laser transition (for a certain light polarization, $\boldsymbol{E} \parallel \boldsymbol{b}$). There are two main reasons for the observed strong anisotropy of the transition cross-sections (absorption and stimulated-emission) of Nd^{3+} ions in CsGdMo, namely, (i) the low symmetry of the rare-earth site (C_2) and (ii) the layered structure of this monoclinic host matrix.

4.4. Laser set-up

To fabricate the laser element, we used a crystal boule grown along the [100] direction. A thin crystal plate (thickness: t = 1.39 mm) was obtained by mechanical cleavage along the (100) plane. It was consequently oriented for light propagation along the ***a***-axis (***a***-cut). The clean aperture of the crystal plate was >1 cm^2. No polishing or coatings were applied. The parallelism of the cleaved crystal faces was measured using a goniometer to be about 1" (angular second). The surface roughness of the cleaved faces was below 50 nm. The crystal plate was fixed on a Cu-holder from below and it was passively cooled.

The plano-plano (microchip) laser cavity, Fig. 10, consisted of a plane pump mirror (PM) coated for high transmission (HT, T > 94%) at 0.81 μm and for high reflection (HR) at 1.02-1.10 μm, and a set of flat output couplers (OCs) with a transmission at the laser wavelength T_{OC} of 1%–15%. Both the PM and OC pressed the crystal plate eliminating the air gaps. As a pump source, we used a CW Ti:Sapphire laser (3900S, Spectra Physics) delivering up to 3 W at λ_P = 808.8 nm in the fundamental mode ($M^2 \approx 1$). The pump polarization in the crystal corresponded to ***E*** || ***b***. The pump was focused into the crystal through the PM using an uncoated spherical CaF_2 lens (f = 40 mm). The pumping was in a single-pass. The measured pump absorption under lasing conditions η_{abs} was 72±2%.

The laser emission spectra were measured using the OSA. The laser output was filtered from the residual pump using a long-pass filter (FEL1000, Thorlabs).

4.5. Laser performance

The input-output dependences of the Nd:CsGdMo laser are shown in Fig. 11(a). The laser generated a maximum output power of 0.54 W at 1066 nm (at an absorbed pump power P_{abs} of 1.13 W) with a slope efficiency η of 60.4%. The laser threshold was at P_{th} = 70 mW and the optical-to-optical efficiency η_{opt} amounted to 47.8% (vs. the absorbed pump power). These characteristics were measured for T_{OC} = 10%. For smaller T_{OC}, the laser efficiency deteriorated, however, even lower laser thresholds (down to P_{th} = 37 mW for T_{OC} = 1%) were observed. No crystal fracture was observed. However, for P_{abs} > 0.9 W, a thermal roll-over was observed in the input-output dependences due to the passive cooling of the crystal-plate. The laser operated for >1 hour without any noticeable degradation of the output performance. The power fluctuations were <5%.

The laser emission was linearly polarized (***E*** || ***b***) in agreement with the anisotropy of the SE cross-sections, Fig. 8. Typical spectra of the laser emission are shown in Fig. 11(b). For small output coupling (T_{OC} = 1%), several emission lines at 1066, 1074 and 1083 nm were observed, which correspond to the local peaks in the σ_{SE} spectra for ***E*** || ***b***, Fig. 8. For T_{OC} > 5%, the laser emitted a single line centered at 1066 nm. The emission bandwidth was ~2 nm.

The laser mode profile measured in the far-field is shown in the inset of Fig. 11(a). It is slightly multi-mode with the measured beam quality parameters M^2_x = 1.8, M^2_y = 1.2 (for an intermediate pump power P_{abs} = 0.6 W). With increasing the pump level, the generation of

higher-order modes was promoted which is typical for Nd microchip lasers; the measured M^2 parameters were below 3.

The fabricated laser elements showed high optical homogeneity, as indicated by well-preserved laser performance while moving the pump spot across the clear aperture of the sample.

The laser operation in a plano-plano cavity indicates positive (focusing) thermal lens in ***a***-cut Nd:CsGdMo crystals. Due to its layered structure, the thermal conductivity of CsGdMo is anisotropic. It is expected to be much higher in the layer plane which is favorable for the studied laser geometry. Indeed, for relatively short laser elements with longitudinal pumping and strong pump absorption, the heat transfer is predominantly transversal.

Recently, we studied the laser properties of another molybdate crystal with a layered structure – orthorhombic Nd:$KY(MoO_4)_2$ [49]. It exhibited negative thermal lens (for the ***c***-cut orientation) thus preventing the microchip laser design. Using a bulk laser element and a similar pump scheme, this laser generated a peak power of 0.55 W at 1067 nm with η = 64% and a laser threshold of 50 mW (quasi-CW laser operation). Thus, Nd:CsGdMo provides a similar behavior while in true CW operation regime. Earlier, we also studied the monoclinic Nd:$KGd(WO_4)_2$ crystal [7] in a microchip laser cavity using a bulk N_g-cut sample. This crystal provided higher slope efficiency but lower output power (output power: 0.34 W at 1068 nm with η = 74% and a laser threshold of 80 mW); it exhibited high risk of thermal fracture limiting the output power, even under water-cooling.

5. Conclusions

To conclude, the monoclinic (sp. gr. *P*2/*c*) Nd:$CsGd(MoO_4)_2$ is a promising double molybdate compound for laser applications. This is because of the following advantageous properties. First, the presence of a single substitutional rare-earth site facilitates its doping. The stoichiometric composition $CsNd(MoO_4)_2$ is also feasible. Second, it exhibits a perfect cleavage along the (100) plane due to the layered crystal structure allowing for simple fabrication of high optical quality crystal plates and (potentially) crystal films with a thickness down to hundreds of microns. Third, the layered crystal structure and the low symmetry of the crystal-field in the rare-earth site (C_2) lead to strongly anisotropic spectroscopic properties, namely, high absorption and stimulated-emission cross-sections with polarized light. This is a prerequisite for linearly polarized laser output. Fourth, relatively long Gd|Nd-Gd|Nd interatomic distances determine weak cross-talk of the active ions. In addition, this crystal provides high (close to unity) luminescence quantum yield. Finally, Nd:$CsGd(MoO_4)$ possesses a positive thermal lens.

In the present work, we demonstrated the first laser operation of mechanically cleaved crystal-plates of Nd:$CsGd(MoO_4)_2$ in a microchip-type laser cavity. The laser delivered up to 0.54 W at 1066 nm with a high slope efficiency of 60.4% featuring low laser threshold of 70 mW and a linearly polarized laser emission. Further studies should focus on diode-pumped laser operation of Nd:$CsGd(MoO_4)_2$ potentially supporting power scalability. The proposed concept for fabrication of the laser elements can be used for $CsGd(MoO_4)_2$ crystals doped with other rare-earth ions, such as ytterbium (Yb^{3+}).

Acknowledgements

Spanish Government (MAT2016-75716-C2-1-R (AEI/FEDER,UE), Generalitat de Catalunya (2017SGR755).

References

1. P.V. Klevtsov, R.F. Klevtsova, Polymorphism of the double molybdates and tungstates of mono- and trivalent metals with the composition $M^{+}R^{3+}(EO_4)_2$, J. Struct. Chem. 18 (1977) 339-355 [transl. from Zhurnal Strukturnoi Khimii, 18 (1977) 419-439].

2. V. Petrov, M. C. Pujol, X. Mateos, Ò. Silvestre, S. Rivier, M. Aguiló, R. M. Solé, J. H. Liu, U. Griebner, F. Díaz, Growth and properties of $KLu(WO_4)_2$, and novel ytterbium and thulium lasers based on this monoclinic crystalline host, Laser Photon. Rev. 1 (2007) 179-212.

3. J.M. Cano-Torres, M. Rico, X. Han, M.D. Serrano, C. Cascales, C. Zaldo, V. Petrov, U. Griebner, X. Mateos, P. Koopmann, C. Kränkel, Comparative study of crystallographic, spectroscopic, and laser properties of Tm^{3+} in $NaT(WO_4)_2$ (T = La, Gd, Y, and Lu) disordered single crystals, Phys. Rev. B 84 (2011) 174207-1–15.

4. M.C. Pujol, M.A. Bursukova, F. Guell, X. Mateos, R. Sole, J. Gavalda, M. Aguilo, J. Massons, F. Diaz, P. Klopp, U. Griebner, V. Petrov, Growth, optical characterization, and laser operation of a stoichiometric crystal $KYb(WO_4)_2$, Phys. Rev. B 65 (2002) 165121-1-11.

5. Y. Chen, Y. Lin, X. Gong, Q. Tan, J. Zhuang, Z. Luo, Y. Huang, Polarized spectroscopic properties of Nd^{3+}-doped $KGd(WO_4)_2$ single crystal, J. Lumin. 126 (2007) 653-660.

6. O. Silvestre, M. C. Pujol, M. Rico, F. Güell, M. Aguiló, and F. Díaz, "Thulium doped monoclinic $KLu(WO_4)_2$ single crystals: growth and spectroscopy," Appl. Phys. B 87 (2007) 707–716.

7. X. Mateos, P. Loiko, J.M. Serres, K. Yumashev, U. Griebner, V. Petrov, M. Aguiló, F. Díaz, Efficient micro-lasers based on highly-doped monoclinic double tungstates, IEEE J. Quantum Electron. 53 (2017) 1700110-1-10.

8. T.T. Basiev, A.A. Sobol, Y.K. Voronko, P.G. Zverev, Spontaneous Raman spectroscopy of tungstate and molybdate crystals for Raman lasers, Opt. Mater. 15 (2000) 205-216.

9. P. Loiko, S.J. Yoon, J.M. Serres, X. Mateos, S.J. Beecher, R.B. Birch, V.G. Savitski, A.J. Kemp, K. Yumashev, U. Griebner, V. Petrov, M. Aguiló, F. Díaz, J.I. Mackenzie, Temperature-dependent spectroscopy and microchip laser operation of $Nd:KGd(WO_4)_2$, Opt. Mater. 58 (2016) 365-372.

10. J. Liu, V. Petrov, X. Mateos, H. Zhang, and J. Wang, Efficient high-power laser operation of $Yb:KLu(WO_4)_2$ crystals cut along the principal optical axes, Opt. Lett. 32 (2007) 2016–2018.

11. J.M. Serres, X. Mateos, P. Loiko, K. Yumashev, N. Kuleshov, V. Petrov, U. Griebner, M. Aguiló, F. Díaz, Diode-pumped microchip $Tm:KLu(WO_4)_2$ laser with more than 3 W of output power, Opt. Lett. 39 (2014) 4247–4250.

12. V. Jambunathan, X. Mateos, M.C. Pujol, J.J. Carvajal, F. Díaz, M. Aguiló, U. Griebner, V. Petrov, Continuous-wave laser generation at ~2.1 μm in $Ho:KRE(WO_4)_2$ (RE = Y, Gd, Lu) crystals: a comparative study, Opt. Express 19 (2011) 25279-25289.

13. A.A. Demidovich, A.P. Shkadarevich, M.B. Danailov, P. Apai, T. Gasmi, V.P. Gribkovskii, A.N. Kuzmin, G.I. Ryabtsev, L.E. Batay, Comparison of cw laser performance of Nd:KGW, Nd:YAG, Nd:BEL, and $Nd:YVO_4$ under laser diode pumping, Appl. Phys. B 67 (1998) 11-15.

14. O. Musset, J.P. Boquillon, Comparative laser study of Nd:KGW and Nd:YAG near 1.3 μm, Appl. Phys. B 64 (1997) 503-506.

15. P.A. Loiko, K.V. Yumashev, N.V. Kuleshov, V.G. Savitski, S. Calvez, D. Burns, A.A. Pavlyuk, Thermal lens study in diode pumped N_g- and N_p-cut $Nd:KGd(WO_4)_2$ laser crystals, Opt. Express 17 (2009) 23536-23543.

16. A.A. Demidovich, A.S. Grabtchikov, V.A. Lisinetskii, V.N. Burakevich, V.A. Orlovich, W. Kiefer, Continuous-wave Raman generation in a diode-pumped Nd^{3+}:$KGd(WO_4)_2$ laser, Opt. Lett. 30 (2005) 1701-1703.
17. J. Huang, J. Lin, R. Su, J. Li, H. Zheng, C. Xu, F. Shi, Z. Lin, J. Zhuang, W. Zeng, W. Lin, Short pulse eye-safe laser with a stimulated Raman scattering self-conversion based on a Nd:KGW crystal, Opt. Lett. 32 (2007) 1096-1098.
18. A.J. Lee, H.M. Pask, D.J. Spence, J.A. Piper, Generation of yellow, continuous-wave emission from an intracavity, frequency-doubled Nd:KGW self-Raman laser, in Advanced Solid-State Photonics 2010, (Optical Society of America, 2010), paper ATuA22.
19. P. Shi, Z. Xia, M.S. Molokeev, V.V. Atuchin, Crystal chemistry and luminescence properties of red-emitting $CsGd_{1-x}Eu_x(MoO_4)_2$ solid-solution phosphors, Dalton Trans. 43 (2014) 9669-9676.
20. W. Zhao, Y.S. Huang, Z.B. Lin, B. Wei, F.W. Wang, M. Xu, X. Zhao, Q.-H. Zheng, W.-W. Zhou, Spectra and energy levels of a layered Yb^{3+}:$CsGd(MoO_4)_2$ crystal with perfect cleavage: a candidate for microchip lasers, RSC Adv. 5 (2015) 34730-34736.
21. N. V. Ivannikova, L.P. Kozeeva, A.A. Pavlyuk, Solubility and growth of $CsGd(MoO_4)_2$ single crystals, Inorg. Mater. 24 (1988) 379-383 [transl. from Izv. Akad. Nauk SSSR, Neorg. Mater. 24 (1988) 466-469]
22. V. Tkáč, A. Orendáčová, R. Tarasenko, E. Čižmár, M. Orendáč, K. Tibenská, A.G. Anders, S. Gao, V Pavlik, A. Feher, Multiple-timescale relaxation dynamics in $CsGd(MoO_4)_2$ - a dipolar magnet with a highly anisotropic layered crystal structure, J. Phys.: Cond. Matter 25 (2013) 506001-1-10.
23. J. Liu, W. Han, X. Chen, D. Zhong, B. Teng, C. Wang, Y. Li, Spectroscopic properties and continuous-wave laser operation of Yb:$LuPO_4$ crystal, Opt. Lett. 39 (2014) 5881-5884.
24. H. Zhu, Y. Chen, Y. Lin, X. Gong, Q. Tan, Z. Luo, Y. Huang, Growth, spectral properties, and laser demonstration of Yb^{3+}:$BaGd_2(MoO_4)_4$ cleavage crystal, J. Appl. Phys. 101 (2007) 063109-1-8.
25. R.F. Klevtsova, V.A. Vinokurov, P.V. Klevtsov, Crystal structure and thermal stability of $CsPr(MoO_4)_2$, Sov. Phys.: Crystallogr. 17 (1972) 240 [transl. from Kristallografiya 17 (1972) 284-288].
26. A.A. Pavlyuk, L.I. Kozeeva, K.G. Folin, V.G. Gladyshev, V.S. Gulyaev, V.S. Pivtsov, A.A. Kaminskii, Stimulated-emission of the transition $^4F_{3/2} \rightarrow {}^4I_{11/2}$ of Nd^{3+} ions in $RbNd(MoO_4)_2$ and $CsNd(MoO_4)_2$, Inorg. Mater. 19 (1983) 767-768 [transl. from Izv. Akad. Nauk SSSR, Neorg. Mater. 19 (1983) 843-848.
27. V. Tkáč, K. Tibenska, A. Orendáčová, M. Orendáč, A.G. Anders, V. Pavlík, A. Feher, The rare-earth based single-ion magnet $CsNd(MoO_4)_2$, Acta Phys. Polon. A. 125 (2014) 244-245.
28. K. Tibenská, V. Tkáč, A. Orendáčová, M. Orendáč, A. Feher, J. Šebek, V. Sechovský, Thermal conductivity of a layered $CsGd(MoO_4)_2$ crystal, Acta Phys. Polon. A. 118 (2010) 971-972.
29. P. Stefányi, A. Feher, A. Orendáčová, E.E. Anders, A.I. Zvyagin, The magnetic phase transition in layered cesium rare earth metal dimolybdates, J. Physique 50 (1989) 1297-1299.
30. B. Devakumar, P. Halappa, C. Shivakumara, Dy^{3+}/Eu^{3+} co-doped $CsGd(MoO_4)_2$ phosphor with tunable photoluminescence properties for near-UV WLEDs applications, Dyes Pigm. 137 (2017) 244-255.
31. K. Li, R. Van Deun, Mutual energy transfer luminescent properties in novel $CsGd(MoO_4)_2$: Yb^{3+}, Er^{3+}/Ho^{3+} phosphors for solid-state lighting and solar cells, Phys. Chem. Chem. Phys. 21 (2019) 4746-4754.
32. A. Le Bail, Whole powder pattern decomposition methods and applications: A retrospection, Powder Diffraction 20 (2005) 316-326.

33. M.C. Pujol, R. Solé, J. Massons, J. Gavaldà, X. Solans, C. Zaldo, F. Díaz, M. Aguiló, Structural study of monoclinic $KGd(WO_4)_2$ and effects of lanthanide substitution, J. Appl. Cryst. 34 (2001) 1-6.
34. P.A. Loiko, K.V. Yumashev, N.V. Kuleshov, G.E. Rachkovskaya, A.A. Pavlyuk, Detailed characterization of thermal expansion tensor in monoclinic $KRe(WO_4)_2$ (where Re = Gd, Y, Lu, Yb), Opt. Mater. 34 (2011) 23-26.
35. B.R. Judd, Optical absorption intensities of rare-earth ions, Phys. Rev. 127 (1962) 750–761.
36. G.S. Ofelt, Intensities of crystal spectra of rare-earth ions, J. Chem. Phys. 37, 511–520 (1962).
37. A. A. Kornienko, A. A. Kaminskii, and E. B. Dunina, Dependence of the line strength of f–f transitions on the manifold energy. II. Analysis of Pr^{3+} in $KPrP_4O_{12}$, Phys. Status Solidi B 157 (1990) 267-273.
38. P. Loiko, A. Volokitina, X. Mateos, E. Dunina, A. Kornienko, E. Vilejshikova, M. Aguilo, F. Diaz, Spectroscopy of Tb^{3+} ions in monoclinic $KLu(WO_4)_2$ crystal: application of an intermediate configuration interaction theory, Opt. Mater. 78 (2018) 495-501.
39. P.A. Loiko, A.S. Yasukevich, A.E. Gulevich, M.P. Demesh, M.B. Kosmyna, B.P. Nazarenko, V.M. Puzikov, A.N. Shekhovtsov, A.A. Kornienko, E.B. Dunina, N.V. Kuleshov, K.V. Yumashev, Growth, spectroscopic and thermal properties of Nd-doped disordered $Ca_9La(VO_4)_7$ and $Ca_{10}(Li/K)(VO_4)_7$ laser crystals, J. Lumin. 137 (2013) 252-258.
40. C. Duan, P.A. Tanner, V.N. Makhov, M. Kirm, Vacuum ultraviolet spectra and crystal field analysis of $YAlO_3$ doped with Nd^{3+} and Er^{3+}, Phys. Rev. B 75 (2007) 195130-1-11.
41. Y. Chen, Y. Lin, X. Gong, Q. Tan, Z. Luo, Y. Huang, Polarized spectral characteristics of Nd^{3+}:$KY(MoO_4)_2$ crystal with perfect cleavage planes: a promising microchip gain medium, J. Opt. Soc. Am. B 24 (2007) 496-503.
42. E. Cavalli, E. Zannoni, C. Mucchino, V. Carozzo, A. Toncelli, M. Tonelli, M. Bettinelli, Optical spectroscopy of Nd^{3+} in $KLa(MoO_4)_2$ crystals, J. Opt. Soc. Am. B 16 (1999) 1958-1965.
43. X. Huang, G. Wang, Growth, thermal and spectroscopic characteristics of Nd^{3+}:$LiGd(MoO_4)_2$ crystal, J. Phys. D: Appl. Phys. 41 (2008) 225401-1-7.
44. L. Wu, Z. Chen, Y. Wu, G.Liu, A. Li, Y. Hao, S. Zhu, L. Zhen, Growth process and optical investigations of Nd:$NaGd(MoO_4)_2$ crystals with varying content of Nd and Gd, Cryst. Res. Technol. 51 (2016) 137-144.
45. Y. Wang, C. Tu, Z. You, J. Li, Z. Zhu, G. Jia, X. Lu, B. Wu, Growth of large-sized Nd:$NY(WO_4)_2$ crystal and its spectral properties, J. Cryst. Growth 285 (2005) 123-129.
46. X. Huang, Z. Lin, Z. Hu, L. Zhang, J. Huang, G. Wang, Growth, structure and spectroscopic characterizations of Nd^{3+}-doped $LiLa(WO_4)_2$ crystal, J. Cryst. Growth 269 (2004) 401-407.
47. A.A. Kaminskii, Laser crystals: their physics and properties, 2nd Ed. (Springer-Verlag, 2013).
48. B. Aull, H. Jenssen, Vibronic interactions in Nd:YAG resulting in nonreciprocity of absorption and stimulated emission cross sections, IEEE J. Quantum Electron. 18 (1982) 925-930.
49. P. Loiko, E. Kifle, J.M. Serres, X. Mateos, M. Aguiló, F. Díaz, E. Vilejshikova, N. Kuleshov, and A. Pavlyuk, Efficient continuous-wave in-band pumped Nd:$KY(MoO_4)_2$ laser, Laser Phys. Lett. 15 (2018) 065002-1-5.

List of figure captions

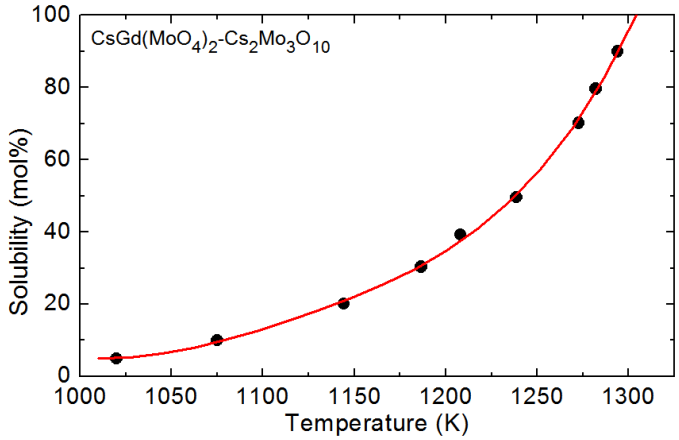

Figure 1. Temperature-dependent solubility of $CsGd(MoO_4)_2$ in the melt with $Cs_2Mo_3O_{10}$.

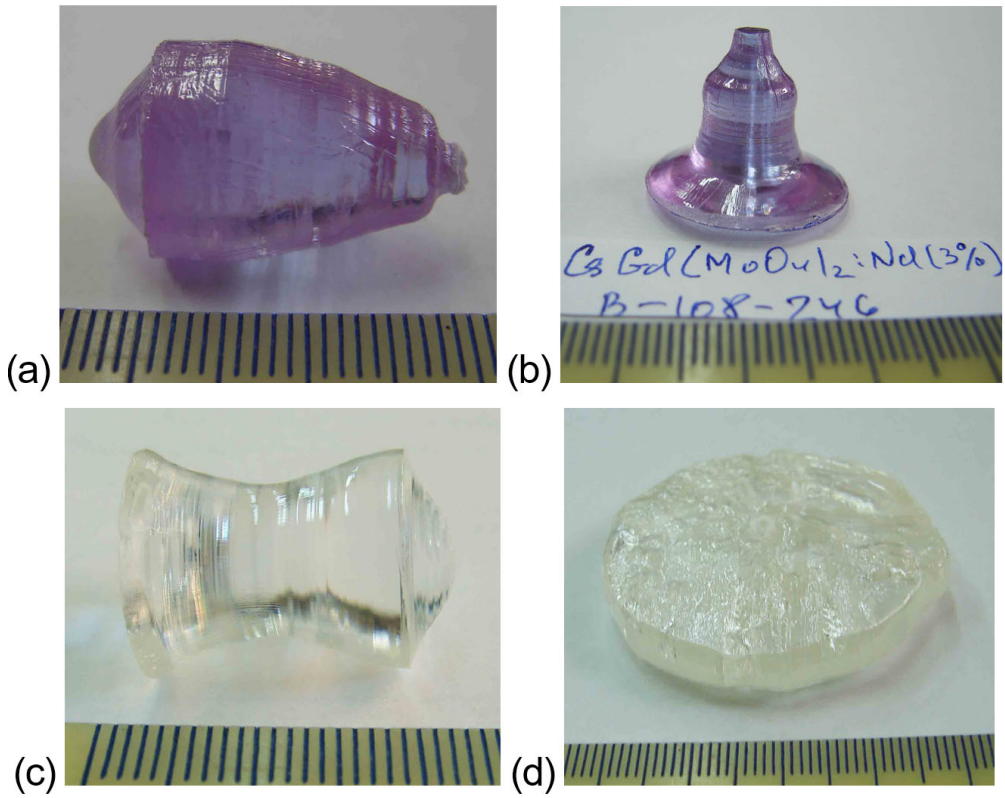

Figure 2. Photographs of the as-grown (a,b) 3 at.% Nd:CsGdMo and (c,d) undoped CsGdMo crystals. (a-c) Growth on an oriented seed crystal. The growth direction is along the (a) [001] axis; (b,c) [100] axis. (d) Growth on a Pt wire.

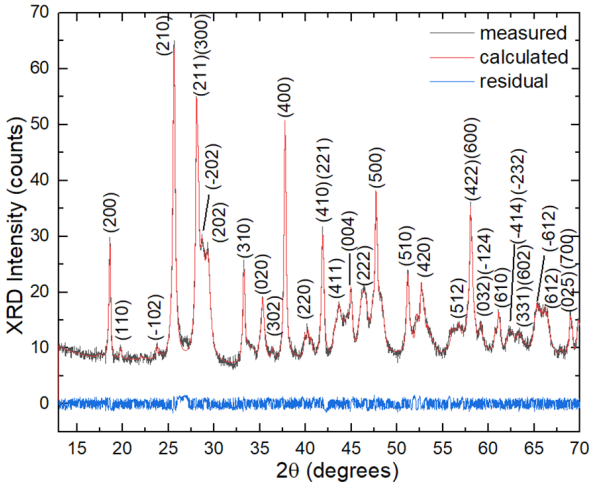

Figure 3. Room-temperature X-ray powder diffraction (XRD) pattern of the 3 at.% Nd:CsGdMo crystal showing Le Bail refinement of the crystal structure.

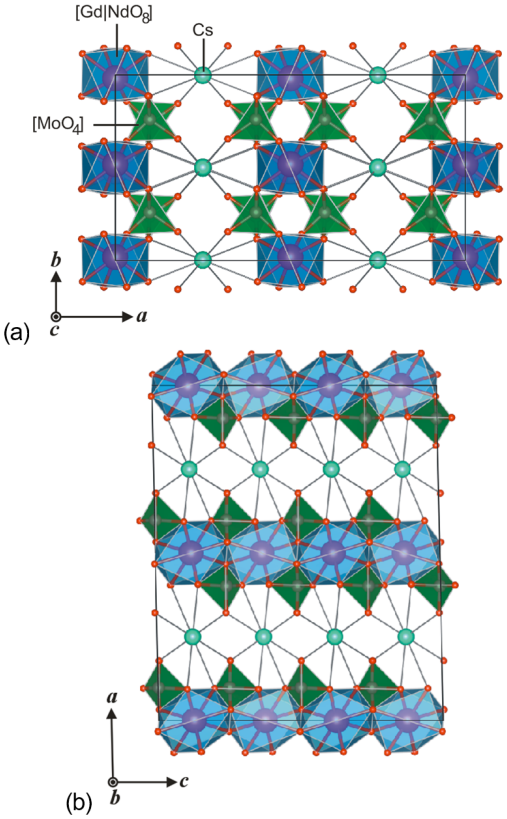

Figure 4. Crystal structure of Nd:CsGdMo: a supercell ($2a \times 2b \times 2c$) in projection to (a) ***a*-*b*** plane, (b) ***a*-*c*** plane.

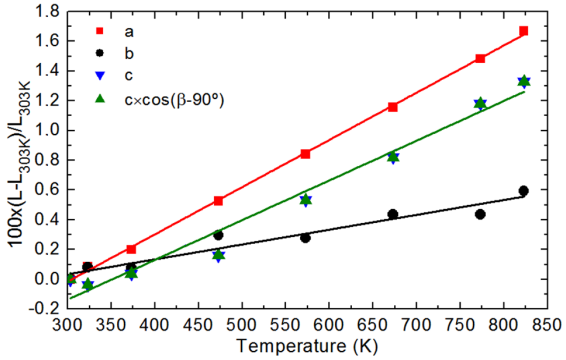

Figure 5. Thermal evolution of the unit cell parameters (L = a, b, c and c^* = c×cos(β–90°)) of 3 at.% Nd:CsGd(MoO_4)$_2$, according to the high-temperature XRD data.

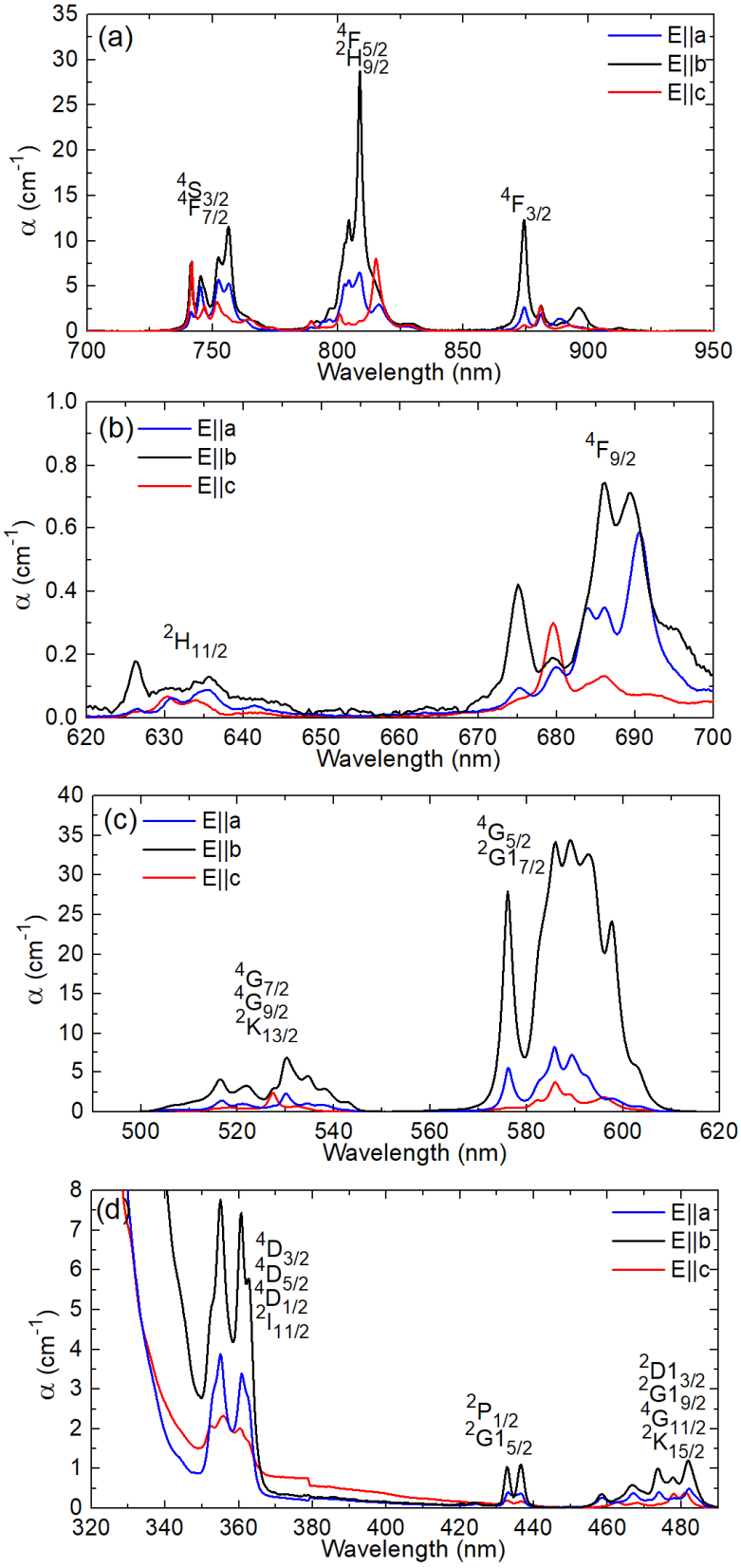

Figure 6. (a-d) Absorption spectra of a 3 at.% Nd:CsGdMo crystal for light polarizations ***E*** || ***a***, ***b***, ***c***.

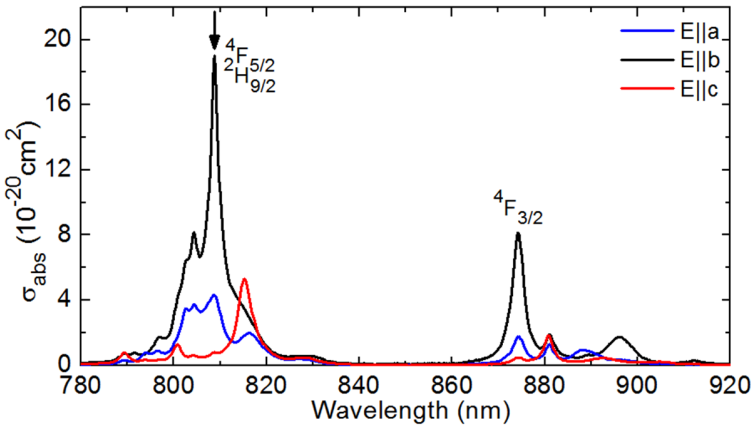

Figure 7. Absorption cross-section, σ_{abs}, spectra for the $^4I_{9/2} \rightarrow {}^4F_{5/2} + {}^2H_{9/2}$ and $^4F_{3/2}$ transitions of Nd^{3+} ions in CsGdMo for light polarizations $\boldsymbol{E} \parallel \boldsymbol{a}$, $\boldsymbol{b}$, $\boldsymbol{c}$. The *arrow* indicates the pump wavelength in the laser experiments.

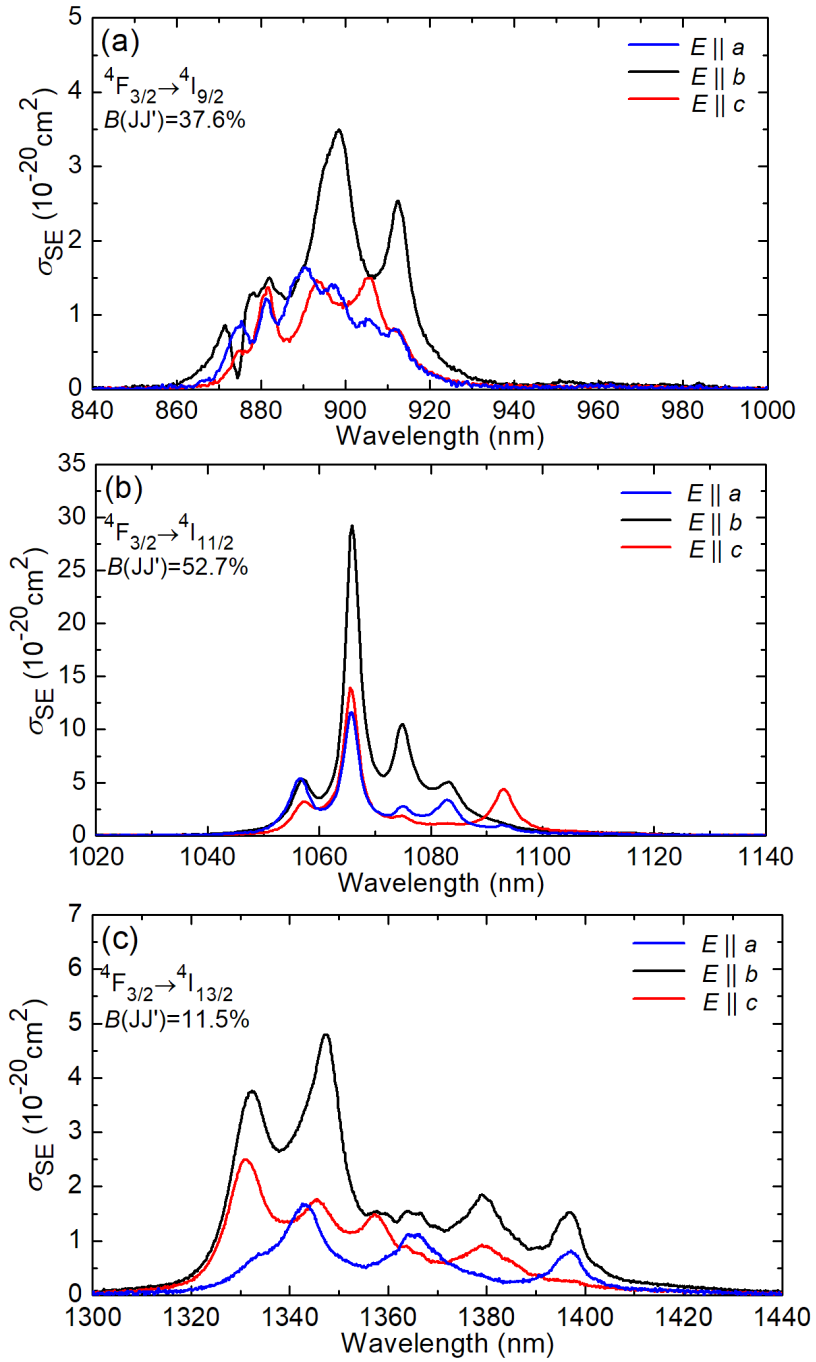

Figure 8. Stimulated-emission (SE) cross-section, σ_{SE}, spectra of Nd^{3+} ions in Nd:CsGdMo: (a) the $^4F_{3/2} \rightarrow {}^4I_{9/2}$ transition; (b) the $^4F_{3/2} \rightarrow {}^4I_{11/2}$ transition and (c) the $^4F_{3/2} \rightarrow {}^4I_{13/2}$ transition. The light polarizations ***E*** || ***a***, ***b***, ***c***.

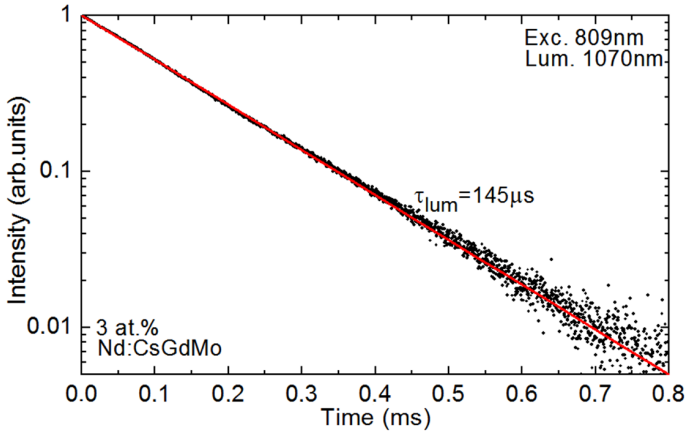

Figure 9. Luminescence decay curve for the 3 at.% Nd:CsGdMo crystal: λ_{exc} = 809 nm, λ_{lum} = 1070 nm.

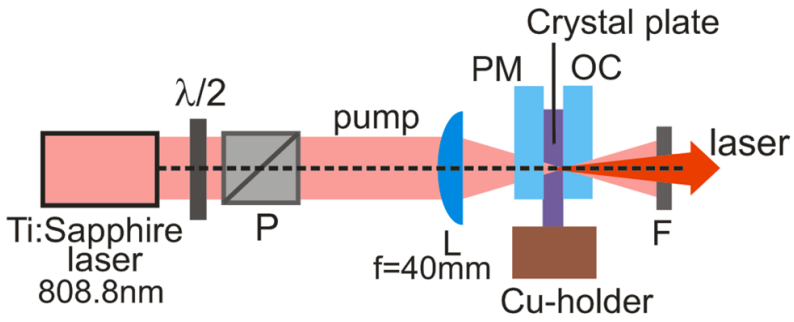

Figure 10. Scheme of the Nd:CsGdMo microchip laser: λ/2 – half-wave plate, P – Glan-Taylor polarizer, L – focusing lens, PM – pump mirror, OC – output coupler, F – long-pass filter.

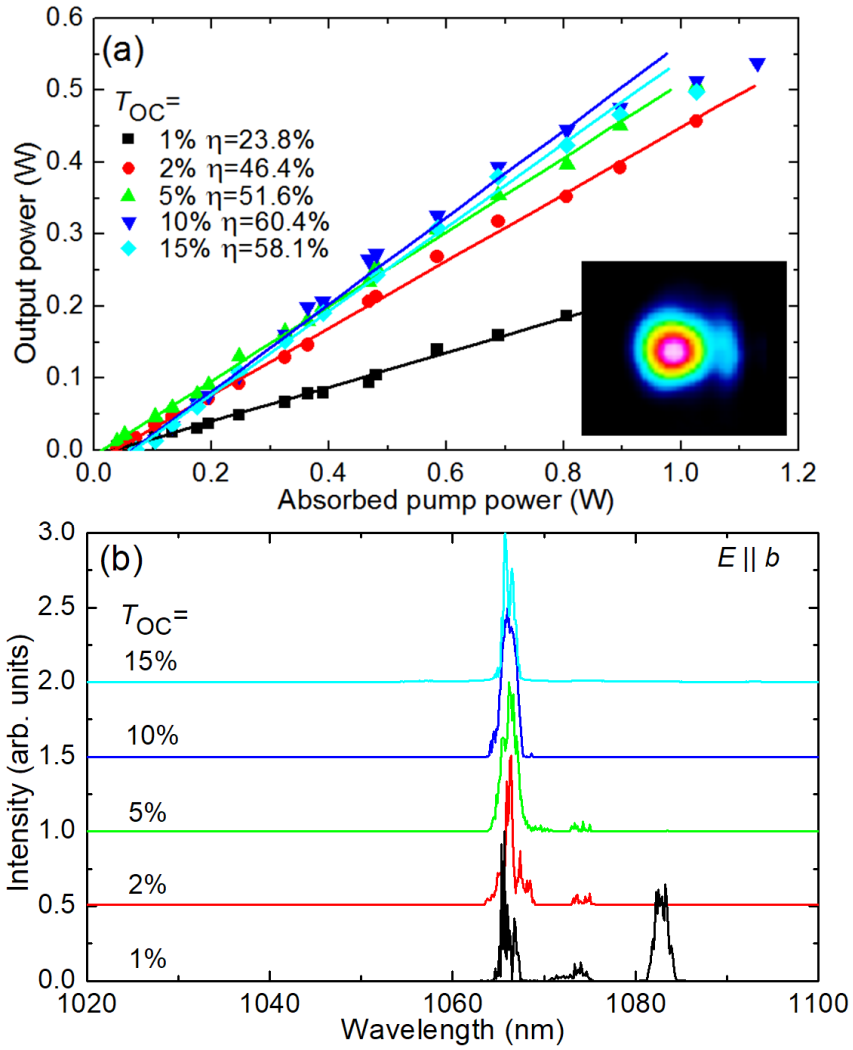

Figure 11. Output characteristics of a microchip laser based on a 1.39 mm-thick cleaved crystal-plate of 3 at.% Nd:CsGdMo: (a) input-output dependences, η – slope efficiency, *inset* – far-field beam profile (T_{OC} = 10%, P_{abs} = 0.6 W); (b) typical laser emission spectra, P_{abs} = 0.9 W. The laser polarization is $\boldsymbol{E} \parallel \boldsymbol{b}$. λ_P = 808.8 nm.